
2022

Aerodynamic Characterization of An Elliptical Fairing In the Wake of a Bluff Body

Luis Amaya
University of Central Florida

STARS Citation

Amaya, Luis, "Aerodynamic Characterization of An Elliptical Fairing In the Wake of a Bluff Body" (2022). *Electronic Theses and Dissertations, 2020-*. 1173.
https://stars.library.ucf.edu/etd2020/1173

AERODYNAMIC CHARACTERISTIZATION OF AN ELLIPTICAL FAIRING IN THE WAKE OF A BLUFF BODY

by

LUIS AMAYA
B.S. Aerospace Engineering, 2020

A thesis submitted in partial fulfillment of the requirements
for the degree of Master of Science in Aerospace Engineering
in the Department of Mechanical and Aerospace Engineering
in the College of Engineering and Computer Science
at the University of Central Florida
Orlando, Florida

Summer Term
2022

Major Professor: Michael Kinzel

ABSTRACT

Aerodynamic optimization is a key step in designing planes, cars, and even buildings. Numerical modeling is used to automate the optimization process and can use different methods to iterate through designs. In this process, consideration of the starting design is paramount as a poor choice can use up computational time and effort. Often, these designs are made with the intention of being out in the open, for which studies on shape variations in freestream situations abound. However, for the case where an object must be placed in the wake of another, there is little research. The study presented here aims to help fill this gap, starting with a case of an elliptical fairing design placed around a cylinder in the wake of a D shaped tube. The fairing itself is parameterized to gain an understanding of how its shape and relative location to the D-tube influence both the fairing itself and the D-tube. The evaluations are done using numerical models that are both validated and measured for uncertainty. Following that, the results are used to provide an initial fairing design for a real case, that being of an instrument on NASA's Dragonfly drone. The example is also used to provide a brief comparison to the trends seen in the 2D characterization as compared to trends seen in freestream design. In total, this research aims to provide a starting point for understanding how design choices affect the aerodynamics of a fairing in a bluff body wake.

TABLE OF CONTENTS

LIST OF FIGURES

LIST OF TABLES

CHAPTER 1: INTRODUCTION

In order to better understand aerodynamics in bluff-body wakes, this effort explores the aerodynamic characterization of an asymmetrical elliptical fairing placed behind a bluff body, specifically that of a D-shaped tube. This generalized characterization study is useful to scenarios involving bluff-body wakes behind many types of bluff bodies such as vehicles or building. In particular, the results can help in the process of choosing an initial fairing shape for optimizing for a similar case as without a proper initial fairing design, time and money can be unnecessarily wasted.

The work here starts by defining the method of shape characterization as the variation of three nondimensional parameters describing the length and thickness of the fairing as well as its distance from the D-tube. An example, using NASA's Dragonfly drone, of a three-dimensional fairing using the results of the characterization is also provided. Following a description of both models and a cursory explanation of the physics models used, a validation and verification effort is performed. For the two-dimensional characterization this takes place in the form of comparing experimental data on a cylinder to both a D-tube and cylinder using the CFD model. The three-dimensional validation uses the automotive bluff Ahmed body to validate and decide on the physics model to be used in the three-dimensional case. Following that, the uncertainty for all studies done are provided. Lastly, the results of the fairing characterization are provided and then applied to the three-dimensional Dragonfly case.

CHAPTER 2: LITERATURE REVIEW

2.1 Bluff Body Wakes

Bluff bodies are a common occurrence, and their related studies have a wide range of applications whether it comes to automobile aerodynamics or even meteorology [1, 2]. Two measures of what makes a body bluff are its large wake and the Strouhal number. The blunt geometry in a bluff body causes the flow to deviate from what is predicted through the base potential flow solution resulting in a large wake. This in turn results in a higher drag due to pressure. From this, the Strouhal number is also affected as this flow separation results in unsteady loads on the body as the result of the periodic shedding of vortices off it. The Strouhal number itself is a function of the frequency of the vortex shedding and it has been experimentally observed that for “bluffer” bodies the Strouhal number is lower [3].

Vortices in general are caused by a difference in flow speed between adjacent regions. This can happen because of a multitude of things, including slower moving flow in boundary layers and because of body geometry such as a sharp corner. When it comes to symmetrical bluff bodies, such as a cylinder, these vortices can form a stable wake at very low Reynolds numbers. At higher Reynolds numbers however, they become unstable and begin to periodically shed from the rear surface of the cylinder. These alternating vortices then form what is known as a von Kármán Vortex Street in the wake of the cylinder [3].

2.2 Fish and Drafting

One area of study that closely relates to the concepts involved here is the intentional use of bluff body wakes to reduce aerodynamic loads. Fish in particular use what is called a Kármán gait when swimming in schools [4] or behind bluff body obstacles. This movement involves a wider amplitude motion than is used for swimming in the freestream flow that matches the positioning of vortices in the trailing von Kármán vortex street. Liao et al hypothesized that by angling their bodies with respect to the vortices allowed them to take advantage of these low-pressure regions to create an upstream force upon each vortex interaction [5, 6].

Another advantage of swimming behind a bluff body is related to a behavior known as entrainment. With this method of swimming, a fish maintains a position within two diameters behind a cylindrical body where the vortices from the bluff body create a flow that is on average pointing upstream. There also exists a similar low-pressure region close to the bluff body, though not all fish use this region as it can lead to a collision [7]. In a similar manner to this, race cars and cyclists take advantage of this low-pressure region to create an advantageous reduction in drag in what is known as drafting or slipstreaming [8] .On top of this, even if a fish is further downstream of the bluff body, it can still take advantage of the overall lower speed created in the wake [7].

2.3 Freestream Airfoils

In contrast to bluff bodies, a streamlined body is capable of maintaining a thin, attached boundary layer over most of its surface [9]. Often this takes on the form of the familiar body of shapes known as airfoils. Airfoils are often described by their characteristics such as their camber, thickness, and the location of the maximum camber or thickness [10]. For the simple characterization study performed here, only the thickness is relevant and is instead referred by its inverse form, the fineness ratio which is taken as the chord divided by the maximum thickness. Concerning fineness, Hoerner showed that for a streamlined body, a value around 3.7 gives an optimally low drag coefficient at a Reynolds number of 10^6. Increasing or decreasing the fineness ratio from this only causes the drag coefficient to increase. This is because for lower fineness ratios the pressure drag is the dominant factor at low fineness ratios, as flow separates more easily from a bluff body such as that of a cylinder, and slowly reduces with increasing fineness. For higher fineness ratios, the friction drag increases as the surface area increases and this eventually overshadows the benefit of maintaining the flow attached [11].

CHAPTER 3: METHODS

3.1 Numerical Modeling

The computational fluid dynamics (CFD) simulation software used here is Siemens' Star-CCM+. For the characterization study, the flow model used is the SIMPLE-C algorithm based segregated solution approach, paired with the implicit unsteady model. The model was chosen under the assumption that the flow is two-dimensional, laminar, and of constant density. With this flow model and assumptions, the conservation equations for mass, momentum, and energy are expressed as:

$$\nabla \cdot v = 0 \tag{1}$$

$$\rho \frac{\partial v}{\partial t} + \rho \nabla \cdot (v \otimes v) = -\nabla \cdot (p\mathbf{I}) + \nabla \cdot \mathbf{T} + f_b \tag{2}$$

$$\frac{\partial (\rho E)}{\partial t} + \nabla \cdot (\rho E v) = \mathrm{f_b} \cdot v + \nabla \cdot (v \cdot \sigma) - \nabla \cdot q + S_E \tag{3}$$

, are solved [12]. Along with this, each case is initialized with a steady version of the model until adequate convergence and is then switched to the transient model. The gas used in the model is based off of air so that $\rho = 1.184\ kg/m^3$ and $\nu = 1.855 \times 10^{-5}\ Pa - s$.

For the three-dimensional trade-study, the flow model used is the SIMPLE-C algorithm based segregated solution approach. The assumptions chosen were that the flow is turbulent and of constant density. For the turbulence, the Reynolds Averaged Navier-Stokes (RANS) model was chosen with Spalart-Allmaras as the eddy viscosity model. From this, the full, unsteady conservation equations given as:

$$\nabla \cdot \bar{v} = 0 \tag{2}$$

$$\rho \frac{\partial}{\partial t}(\bar{v}) + \rho \nabla \cdot (\bar{v} \otimes \bar{v}) = -\nabla \cdot \bar{p}\mathbf{I} + \nabla \cdot (\bar{\mathbf{T}} + \mathbf{T}_{RANS}) + f_b \tag{2}$$

$$\rho \frac{\partial}{\partial t}(\bar{E}) + \rho \nabla \cdot (\bar{E}\bar{v}) = -\nabla \cdot \bar{p}\bar{\boldsymbol{v}} + \nabla \cdot (\bar{\mathbf{T}} + \mathbf{T}_{RANS})\bar{v} - \nabla \cdot \bar{q} + f_b \tag{3}$$

are solved [12]. From this the RANS model is derived by eliminating the transient terms. Here, as the model is meant to represent the Dragonfly cruise phase, the gas used is based off of Titan's atmosphere giving $\rho = 5.35\ kg/m^3$ and $\nu = 6 \times 10^{-6}\ Pa - s$.

$$\nabla \cdot \tilde{v} = 0 \tag{4}$$

$$\rho \frac{\partial}{\partial t}(\tilde{v}) + \rho \nabla \cdot (\tilde{v} \otimes \tilde{v}) = -\nabla \cdot \tilde{p}\mathbf{I} + \nabla \cdot \left(\widetilde{\mathbf{T}} + \mathbf{T}_{SGS}\right) + f_b \tag{5}$$

$$\rho \frac{\partial}{\partial t}\left(\tilde{E}\right) + \rho \nabla \cdot \left(\tilde{E}\tilde{v}\right) = -\nabla \cdot \tilde{p}\tilde{\boldsymbol{v}} + \nabla \cdot \left(\widetilde{\mathbf{T}} + \mathbf{T}_{SGS}\right)\tilde{v} - \nabla \cdot \tilde{q} + f_b\tilde{v} \tag{6}$$

In addition to the URANS/RANS models, the Detached Eddy Simulation (DES) is also considered for the three-dimensional trade-off study, using the same assumptions as before. The DES model is a hybrid solver that uses both the URANS equations and the LES conservation equations which are shown as equations 4-6. The main difference in both approaches is the method of filtering. RANS uses an averaging process to filter out components that fluctuate with time, while LES uses a spatial filtering to eliminate components of variables that are smaller than the local mesh size. DES combines both by using RANS modeling in boundary layers and where turbulent scale lengths are smaller than the mesh size and switches to using LES in regions of larger scale turbulence, such as in largely separated flow, and is more accurate in flow prediction, provided that the mesh in those areas is of a fine enough size to capture relevant turbulence [12].

$$Re_D = \frac{\rho V_\infty D}{\mu} \tag{7}$$

The characterization is repeated for the two diameter-based Reynolds numbers of 6250 and 22500, which are calculated using equation 7. From this, the inputs for the velocity inlet boundary condition is given as 1.958 m/s and 7.05 m/s, using the two-dimensional model. As the three-dimensional trade off study is performed using a different medium and bodies, the velocity is changed so that the Reynolds numbers match, resulting in inputs of 0.0379 m/s and 0.1594 m/s. An additional Reynolds number of approximately 1.4 million was also used to find a third velocity input, giving a case that matches the cruise phase for NASA’s Dragonfly drone.

3.2 Fairing Geometry

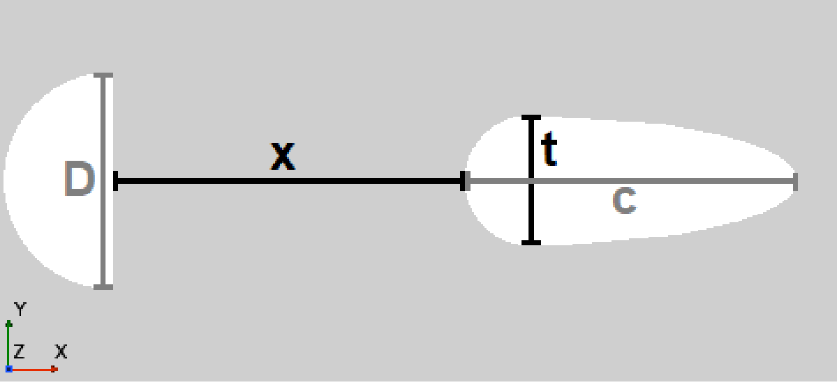

Figure 1: Geometric parameters

For the characterization study, the geometry chosen for the bluff body is that of a D-tube. As a reference, the D-tube has a diameter of 5cm. The fairing is of a rough airfoil shape based off of an asymmetrical ellipse that is modified using three different parameters. First, the fairing is based off of a circle of a diameter “t” whose rear half is extended outward to form a rough airfoil shape of chord length “c.” It is also separated a distance, “x,” from the rear surface of the bluff body. A visual aid showing these parameters is given in figure 1. For the purposes of characterization, the parameters are also nondimensionalized. The separation is given as x/D, the fairing thickness as the ratio t/D, and the length is given as a fineness ratio, set as c/t. Table 1 shows the ranges for the given parameters, with figure 2 showing the maximum case for each parameter. In total, this results in 250 cases at each Reynolds number for the characterization.

(a) Thickness

(b) Distance

(c) Fineness

Figure 2: Maximum and minimum parameter examples

Table 1: Nondimensional parameter ranges

	Lowest Value	Highest Value	Divisions
x/D	0.5	5	5
c/t	1	8	10
t/D	0.2	1	5

3.3 Computational Domain and Mesh

3.3.1 2D Elliptical Fairing Model

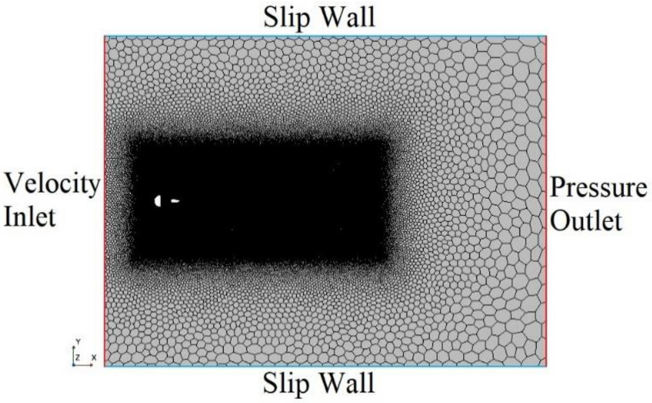

Figure 3: Sample 2D mesh and model domain

As seen in figure 3, for the two-dimensional case the flow enters through a velocity inlet and exits through a pressure outlet. The walls parallel to the flow are modeled as symmetry walls that do not have a no-slip condition. The surfaces of the bodies, however, do have a no-slip condition.

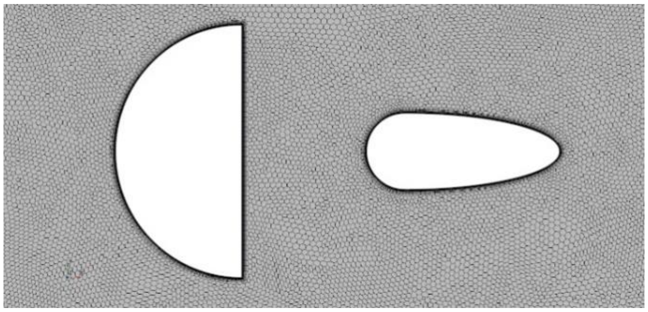

Figure 4: Zoomed-in sample mesh for a case where: x/D = 0.5, t/D = 0.2, and c/t= 2.56

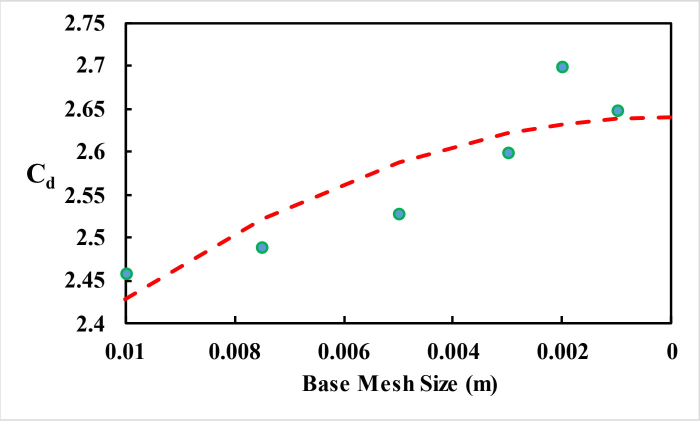

Figure 5: Drag coefficient convergence for D-tube validation

$$C = \frac{V\Delta t}{\Delta x} \tag{8}$$

The numerical uncertainty of the characterization was measured and reduced through a mesh refinement study. For this, the mesh size in the refinement region was varied, while keeping the Courant number in mind. An initial estimate of the Courant number was found through equation 8, though manual adjustment was needed to maintain the Courant number equal to 1 to reach a satisfactory condition in the finer mesh region [13]. For this study, the drag coefficient of the D-tube was used as the measure for convergence. Time averaging of the data was also performed due to the unsteady loads that come with shedding vortices and was done after the flow had reached a steady state where a regular von Kármán vortex street had formed. The region of refinement, seen in figure 3, extends behind the D-tube and fairing so that there is enough space behind both bodies for any given configuration for a von Kármán vortex street to form. Results showing the drag convergence are given in figure 5. The red line represents a least squares fit line generated from the data that shows the drag converging with a decreasing mesh size. From this, a mesh size of 1mm was chosen for the refinement area.

3.3.2 Ahmed Body Model

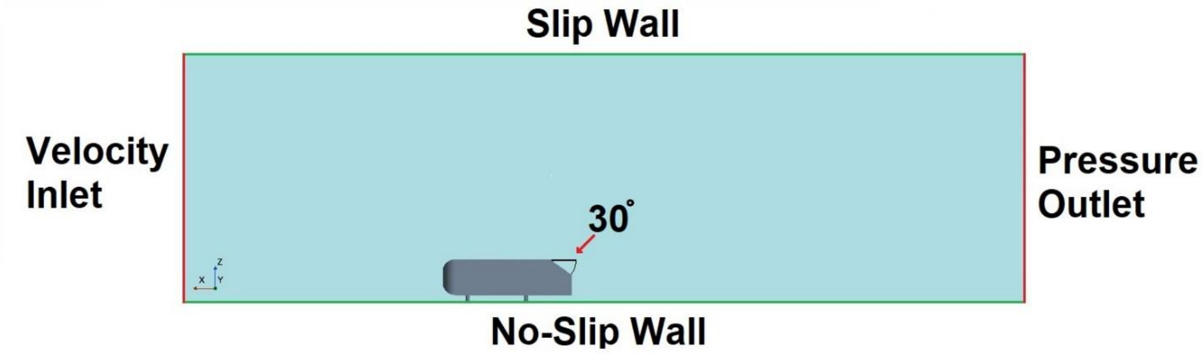

Figure 6: Sideview of Ahmed body domain

For the Ahmed body validation, the domain’s dimensions, seen in figure 6, are set to match the wind tunnel used in the experiment, including the velocity of the flow which was given as 60m/s. Figure 7 shows an example structure of the mesh for the Ahmed body. As a significant portion of the drag on this body is due to pressure drag on the rear faces of the body [15], the mesh refinement focuses on both the surface of the body as well as the wake region. Elsewhere near the body the mesh is double this base size.

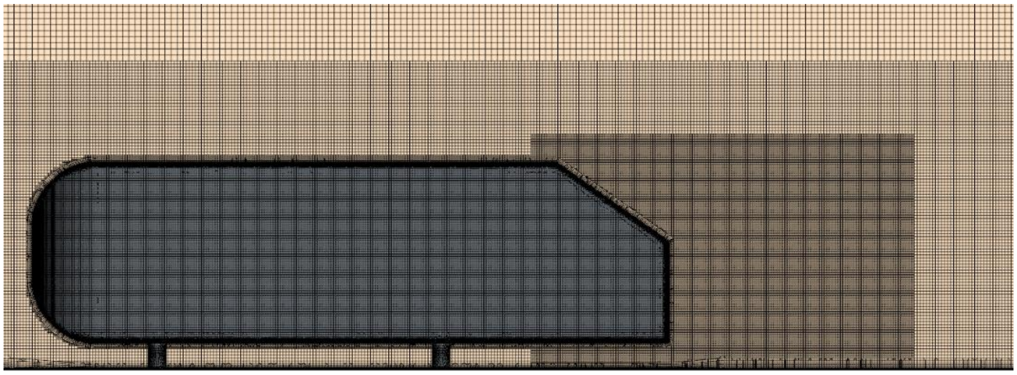

Figure 7: Ahmed body mesh example

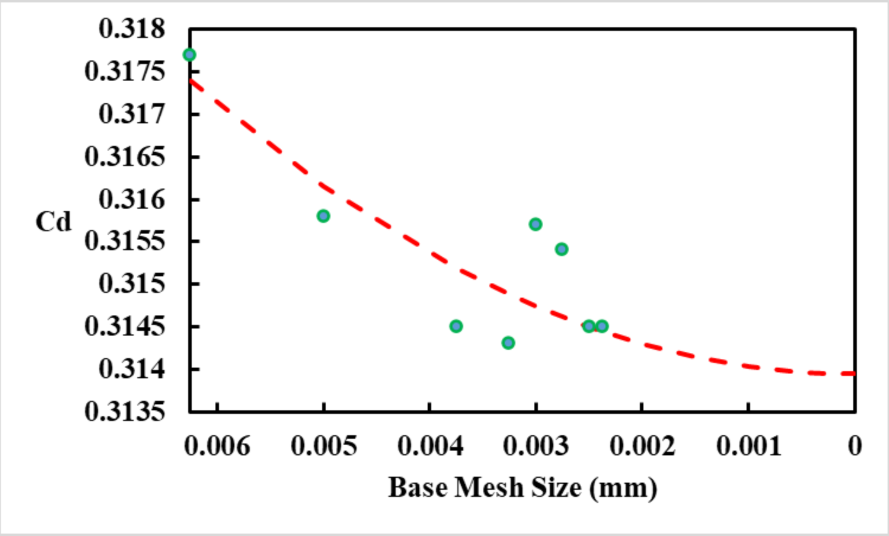

Figure 8: Drag coefficient convergence for Ahmed body

Before the physics model benchmarking for the Ahmed body is done, a mesh refinement is necessary to ensure that any validation this comparison provides is mesh independent. The mesh refinement studies were done using the RANS model. Figure 8 then provides the resulting drag coefficient for the chosen mesh sizes, with the red dash line representing a least squares fit line showing the data converging with a decreasing mesh size. Following these results, a final base size of 2.5mm was chosen.

3.3.3 3D Fairing Example Model

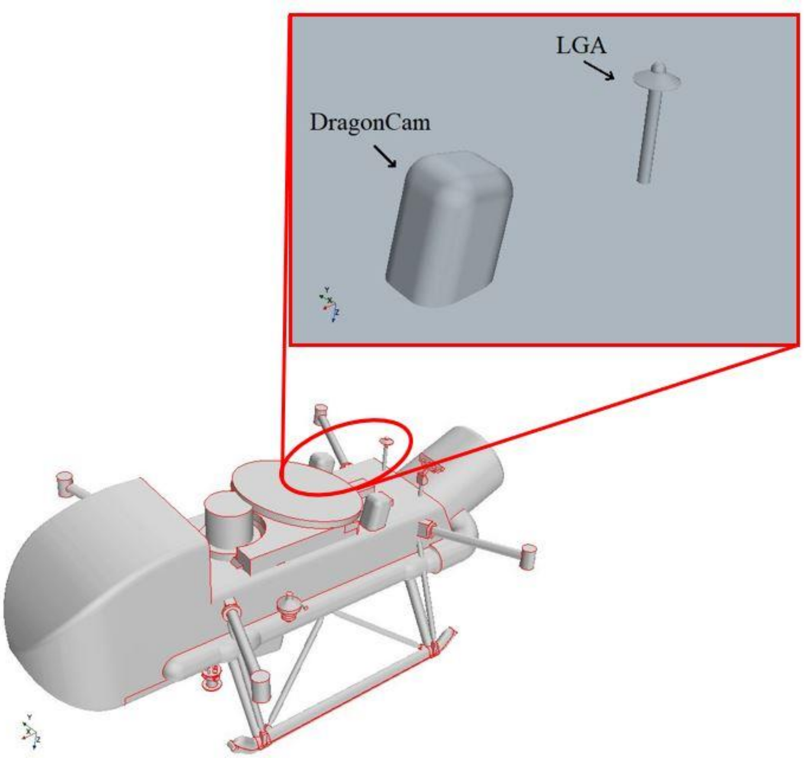

Figure 9: Simplified Dragonfly geometry

For the 3D fairing example, the geometry used is a case derived from NASA's Dragonfly drone. Here, the relevant geometry has been isolated, as well as partially simplified in the case of the Low Gain Antenna, or LGA, as is shown in figure 9. In this case, the bluff body is that of the DragonCam which is situated upstream of the LGA. This case lies within the explored distance and thickness ratios but does differ in two key places. To start, viewed as a cross section, the DragonCam is not a D-tube, but for considering an initial fairing proposal, it is a good match as both are simple bluff bodies. Second, the Reynolds number when calculated using cruise conditions for Dragonfly is of a difference of several orders of magnitude.

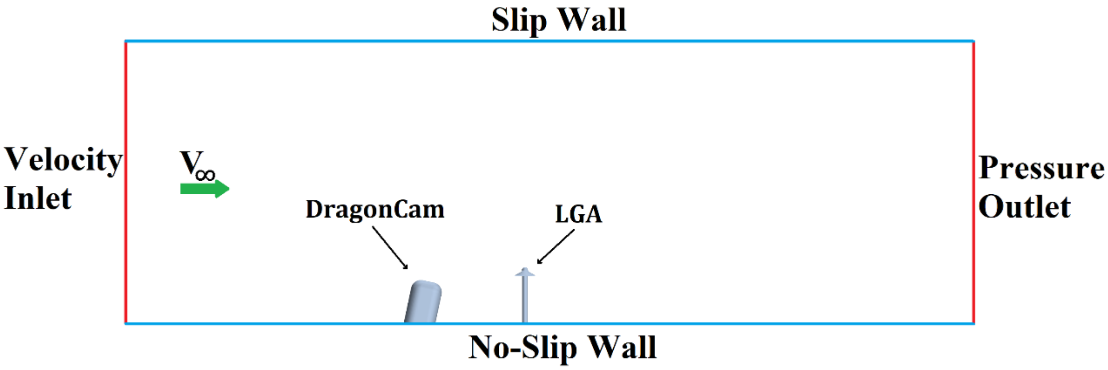

Figure 10: Sideview of 3D Model and Boundaries

The computational domain for the 3D fairing case is shown in figure 10. As with the Ahmed body model, the flow moves from left to right, entering through a velocity inlet, and exiting through a pressure outlet on the right. The walls parallel to the flow, on the top and sides, are set as symmetry walls that allow the flow to slip past with no shear forces. The surface of the DragonCam, LGA, and bottom boundary are set to a no-slip condition. For confidentiality, any provided measurements related to Dragonfly will be normalized on a case-by-case basis.

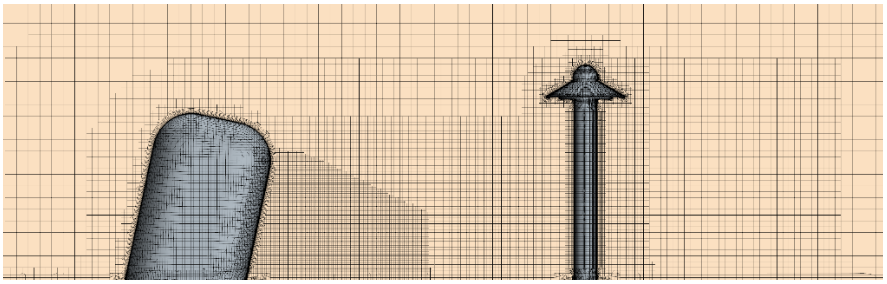

Figure 11: Zoomed-in sample mesh for 3D case

For the 3D fairing case, the numerical uncertainty was evaluated by considering the drag of both the DragonCam and LGA separately. The main refinement regions for the mesh are the surfaces of the bodies and a region in the wake of the DragonCam, similar to what was done with the Ahmed body. Additionally, refinement zones that scale with this size were placed around both bodies to minimize any further wake related uncertainty. An example mesh of the base case with no fairing has been provided in figure 11.

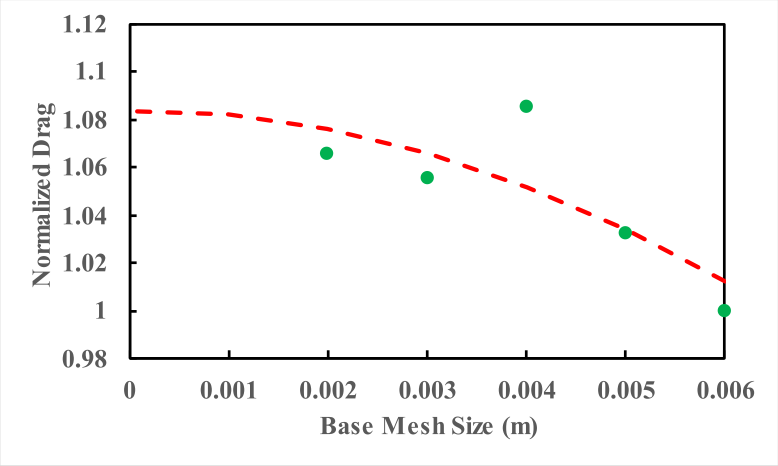

Figure 12: DragonCam Drag Convergence

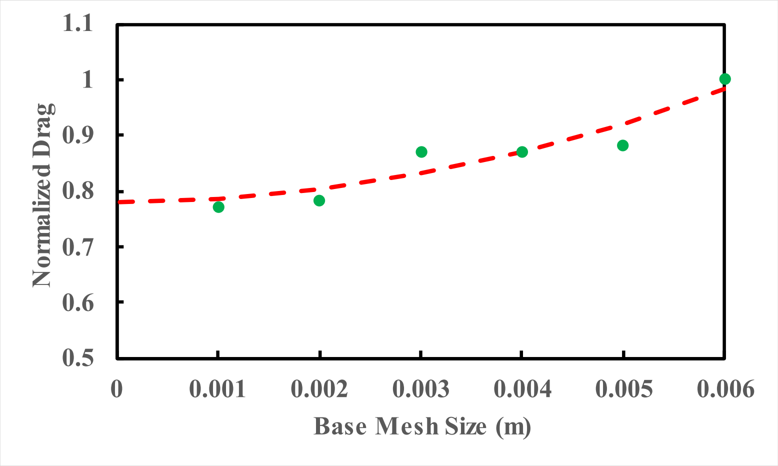

Figure 13: LGA Drag Convergence

Although these studies were run with a steady-state model, the results still had oscillations, so any provided values have been averaged to eliminate this. Figures 12 and 13 provide the mesh convergence results for the DragonCam and LGA. As with the previous mesh refinement studies, a least squares fit line was generated to measure convergence for the bodies, separately. From this, mesh sizes of 4mm and 2mm were chosen for the DragonCam and LGA, respectively.

3.4 Uncertainty

$$U_{total} = \sqrt{U_{numerical}^2 + U_{experimental}^2 + U_{comparison}^2} \tag{9}$$

3.4.1 2D Case Uncertainty

Concerning the uncertainty involved in the two-dimensional wake characterization, the approach taken is a conservative approach. The numerical uncertainty here is measured as twice the difference between the drag at the chosen mesh size and the project value at a mesh size of 0mm. The experimental uncertainty is referenced from Lienhard, who reported a ±5% uncertainty for the Strouhal number using data from various compiled experiments [14]. It is assumed that all of the experimental uncertainty translates directly to uncertainty on drag, using equation 10. Table 2 shows the uncertainty results, as well as the total uncertainty that is calculated using equation 9. Here the comparison uncertainty is not relevant.

Table 2: 2D case drag uncertainty

Numerical (N)	Experimental (N)	Total (N)
±0.132	±0.0005	±0.133

3.4.2 Ahmed Body and 3D Case Uncertainty

Concerning the uncertainty involved with the Ahmed body physics model assessment, the approach taken matches the previous. The numerical uncertainty here is measured as twice the difference between the drag at the chosen mesh size and the project value at a mesh size of 0mm, resulting in ±0.0011 for the drag coefficient uncertainty. The experimental uncertainty is referenced from Ahmed, who reported a ±0.2N uncertainty for the drag [15], translating to an uncertainty of ±0.0008 for the drag coefficient uncertainty. The comparison uncertainty, reported in Table 3, is taken as the difference between a given physics model's prediction and the experimental data, calculated for each slant angle. The total drag uncertainty for each physics model is reported in Table 4.

Table 3: Ahmed body comparison drag coefficient uncertainty

Slant	RANS	URANS	DES
0º	±0.0391	±0.0394	±0.0422
10º	±0.0275	±0.0279	±0.0179
20º	±0.0254	±0.0167	±0.0017
30º	±0.0808	±0.0821	±0.0211

Table 4: Ahmed body total drag coefficient uncertainty

Slant	RANS	URANS	DES
0º	±0.0392	±0.0394	±0.0422
10º	±0.0276	±0.0279	±0.0180
20º	±0.0255	±0.0167	±0.0022
30º	±0.0808	±0.0821	±0.0211

For the uncertainty involved with the three-dimensional fairing example, the approach taken matches the previous. The numerical uncertainty here is measured as twice the difference between the drag at the chosen mesh size and the project value at a mesh size of 0mm, resulting in ±0.0011 for the drag coefficient uncertainty. In this case the experimental uncertainty is not applicable. The comparison uncertainty is taken as the worst-case RANS uncertainty from the Ahmed body study as the same model is used for this study. The total drag coefficient uncertainty for the DragonCam and LGA are reported in Table 5.

Table 5: 3D fairing drag coefficient uncertainty

	Numerical	Comparison	Total
DragonCam	±0.0212	±0.0808	±0.0835
LGA	±0.0290	±0.0808	±0.0858

3.5 Validation Benchmarks

3.5.1 2D Case

$$St = \frac{fD}{U} \qquad (10)$$

To provide confidence in the results generated from the characterization, a validation proving that the model can capture realistic results is necessary. To this end, three cases of an isolated D-tube were run at Reynolds numbers of 6,250, 11,250, 22,500. The vortex shedding frequency was used as the measure for verification. In place of a direct D-tube experimental comparison, the more widely available data on a cylinder is used. Because of this, an additional set of cases have also been generated using the same model where the D-tube is replaced with a cylinder.

$$St = 0.1776 + \frac{2.2023}{\sqrt{Re}} \tag{11}$$

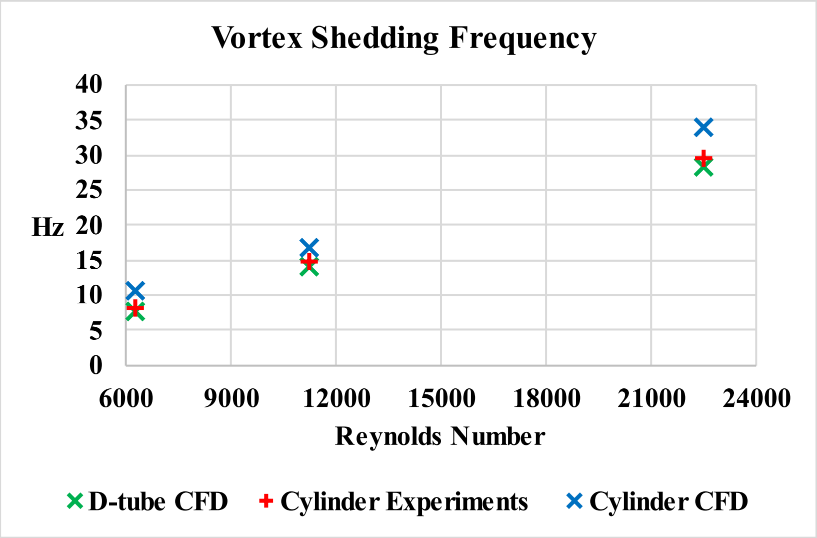

Figure 14: Experimental versus numerical shedding frequency

The experimental data for the Strouhal number was calculated using the experimental results compiled by Lienhard and the relation between the Reynolds and Strouhal numbers provided by Fey, shown as equation 11 for the relevant range of Reynolds numbers [14, 18]. From this, it was found that the Strouhal number is relatively constant at a value of around 0.21. Following this, the vortex shedding frequency is backed out for the chosen Reynolds numbers using equation 10. For the CFD, the vortex shedding frequency is predicted by performing a Fast-Fourier transform on the time varying lift data and extracting the highest frequency. Figure 14 provides the vortex shedding frequency from the CFD results and the experiment-based prediction. Overall, the CFD model is seen to consistently capture the vortex shedding frequency, though there is a bias for the result to be slightly lower than the experimental prediction. The reason for this bias is not clear but given the uncertainty from the Strouhal prediction and the numerical uncertainty, this bias is of low concern.

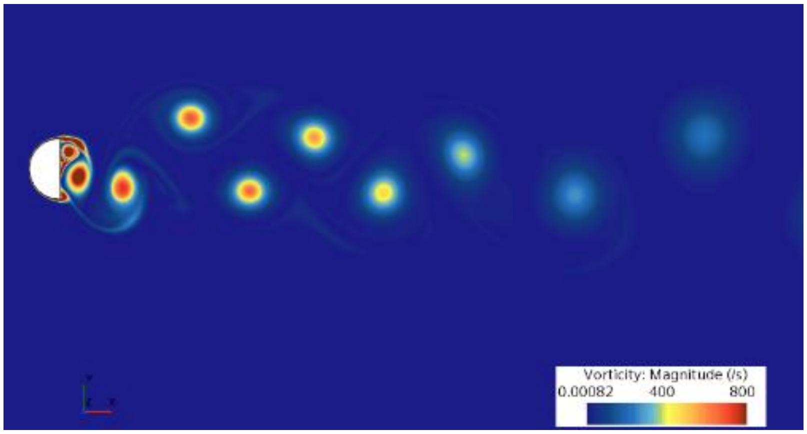

Figure 15: Contour plots of z-direction vorticity at Re = 6,250

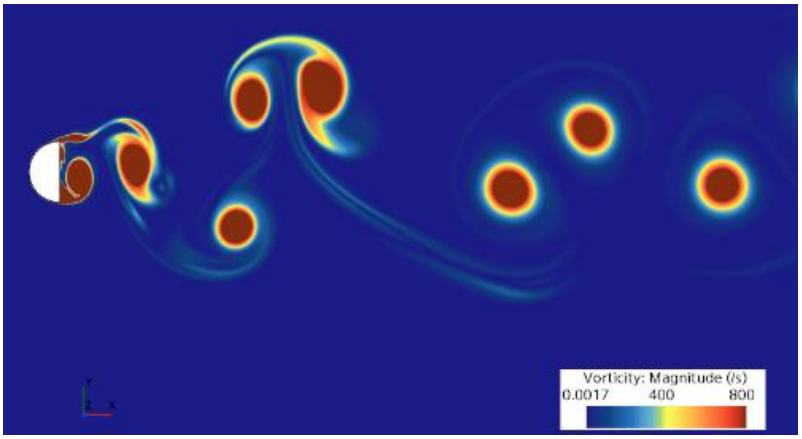

Figure 16: Contour plots of z-direction vorticity at Re = 22,500

Figures 15 and 16 show the developed von Kármán vortex street in the wake of the D-tube. This gives a good indication that the flow model is capable of predicting a realistic flow. Additionally, looking at Table 6 and comparing the CFD predictions, it's clear that the Strouhal number for the D-tube is consistently predicted to be lower than the cylinder's. This matches up with the expectation that a bluffer body results in a lower Strouhal number [3]. Putting this all together, the CFD model can be said to be capable of producing a realistic flow. Moving forward, the characterization is done at the Reynolds numbers of 6,250 and 22,500.

Table 6: CFD based Strouhal numbers

	Re = 6,250	Re = 11,250	Re = 22,500
D-tube	0.1946	0.1986	0.2010
Cylinder	0.2727	0.2396	0.2409

3.5.2 3D Case

Figure 17: Ahmed body geometry

For the three-dimensional case, the validation aims to find the right physics model for a bluff body. For this, the simplified vehicular geometry of the Ahmed body can be used. The Ahmed body consists of a blunt nose, straight sides, and a slanted surface on the back. For the study, the angle at which the surface is at will be varied from 0 to 30 degrees, in increments of 10 degrees, to measure how well a given model can capture varying forms of flow separation. The physics models that will be compared are the RANS, URANS, and DES models.

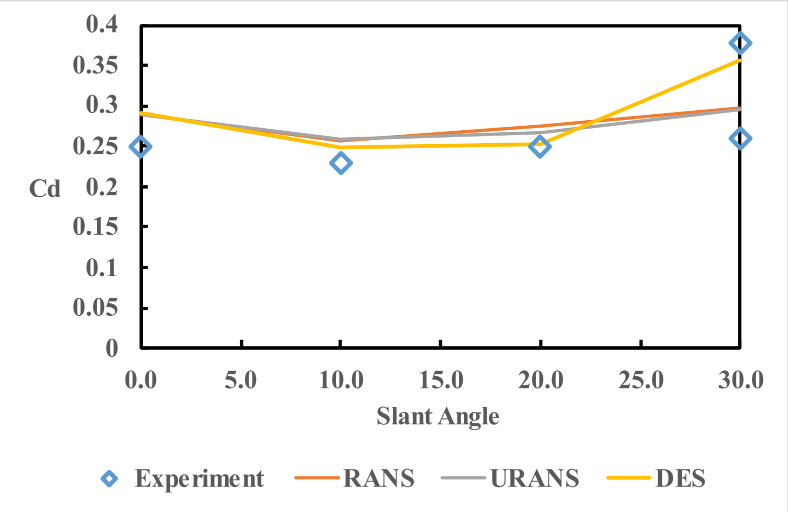

Figure 18: Ahmed body slant angle comparisons

Figure 18 shows the drag coefficient for the Ahmed body variations as compared to the experimental results [15]. As shown, all models manage to capture the behavior seen in the experiment with respect to the changing slant angle. However, there is an overprediction of drag from all models. This is expected as it has previously been found that the Spalart-Allmaras model can lead to an overprediction of drag when it comes to modeling the Ahmed body [16].

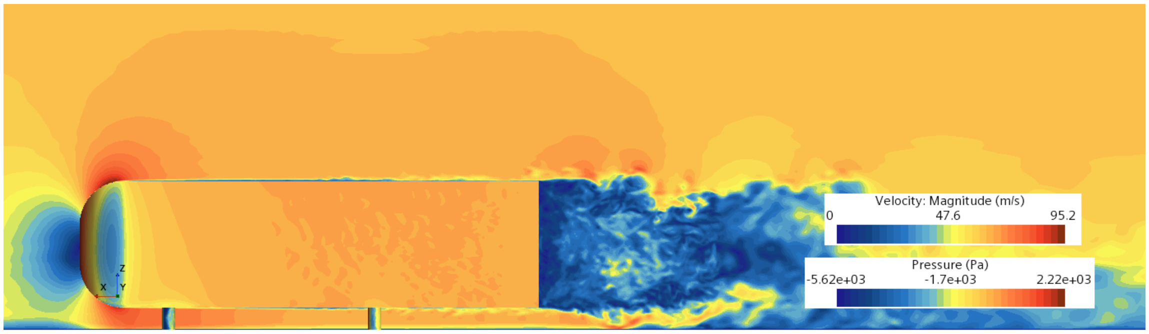

Figure 19: Velocity contour for 0-degree slant Ahmed body using DES

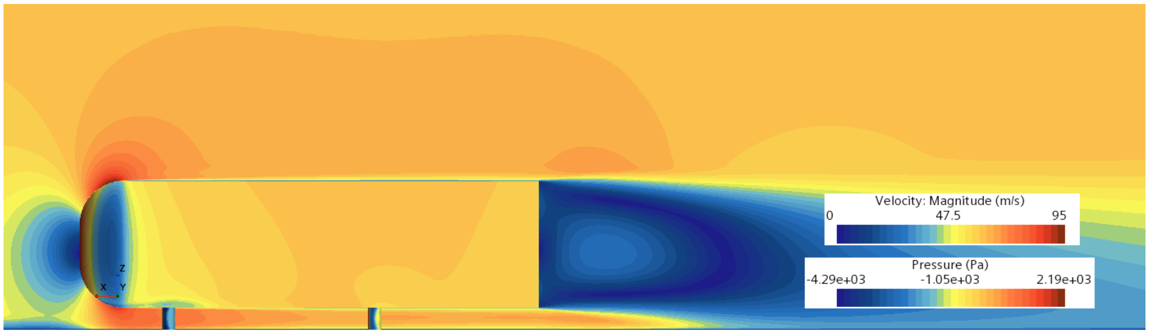

Figure 20: Velocity contour for 0-degree slant Ahmed body using RANS

Something to note, is that the DES model begins to better approach one of the experimental values after a slant angle of 20 degrees. A slant angle of 30 degrees marks a transition point for the Ahmed body where the flow can either remain unattached over the slanted surface and cause the lower experimental drag value, seen in Figure 18, or regions of the wake can merge and cause the flow to attach and result in a higher drag. The RANS and URANS models seem to show a value in between both results, though whether this is accurate is not certain as the lower drag experimental value at this point was surmised to be caused by small disturbances upwind which are not present here [15]. Figures 19 through 22 show these differences through the velocity contours for the DES and URANS models. In figures 21 and 22, the DES model does show the more attached flow for the 30-degree slant case as compared to the URANS model which has the flow fully separated. Despite this fact, however, the goal of the three-dimensional fairing comparison is to capture the trends that come with varying the fairing geometry. Additionally, as the fairing is in the wake of a bluff body, it is not expected that the flow will be so stationary that it will hinge on delicate prediction of flow attachment. Given all of this, the RANS model is sufficient for the three-dimensional fairing comparison.

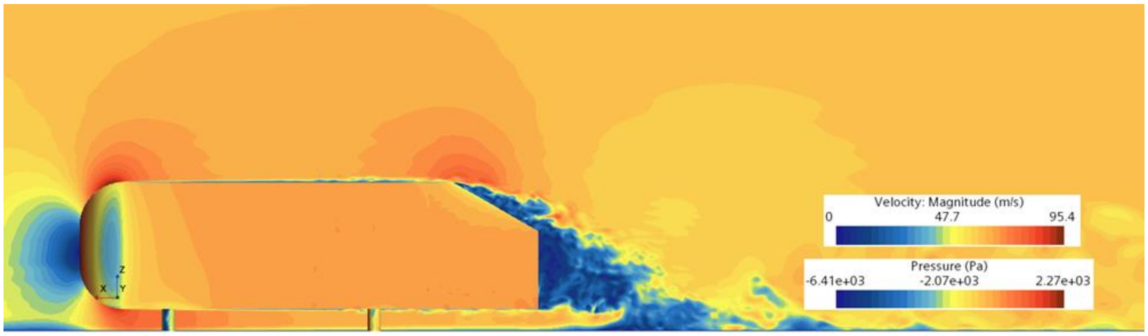

Figure 21: Velocity contour for 30-degree slant Ahmed body using DES

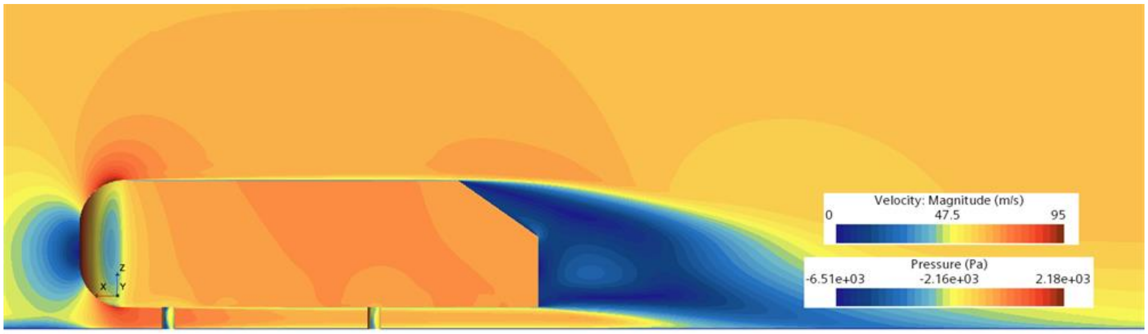

Figure 22: Velocity contour for 30-degree slant Ahmed body using URANS

CHAPTER 4: RESULTS

4.1 Freestream Fairing

To better understand how fairing design in the wake of a bluff body compares to a freestream fairing, the first study involves the fairing exposed to the freestream at the Reynolds numbers of 6,250 and 22,500. For this, only the fineness is a variable and is done from a fineness of 1 up to 10. In each case the drag coefficient is calculated using equation 12.

$$C_d = \frac{D}{\frac{1}{2}\rho V_\infty A_{ref}} \qquad (12)$$

Figures 23 and 24 provide the results of the fineness characterization for the freestream fairing. Both show that in the range of finenesses chosen there exists an optimal fineness. This occurs at finenesses of 6 and 4, for the lower and higher Reynolds numbers.

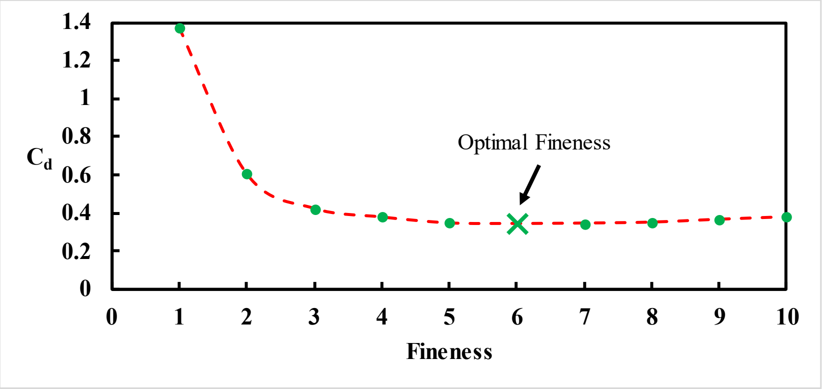

Figure 23: C_d versus fineness in freestream at Re = 6,250

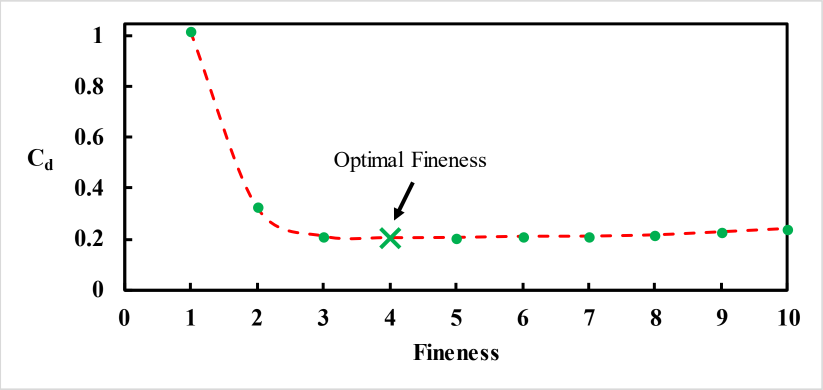

Figure 24: C_d versus fineness in freestream at Re = 22,500

The results can be broken down further by looking into the components of drag. Figures 25 and 26 show the contributions that pressure and shear make in the drag coefficient. Both show that at low finenesses pressure drag is the dominant force, but as the fineness is increased the pressure drag drops and the shear drag increases. This matches what is typically seen with streamlined shapes [11]. It should also be noted that even at the optimal fineness there is still some separation of flow from the fairing at the trailing edge, as the fairing here is rough in design.

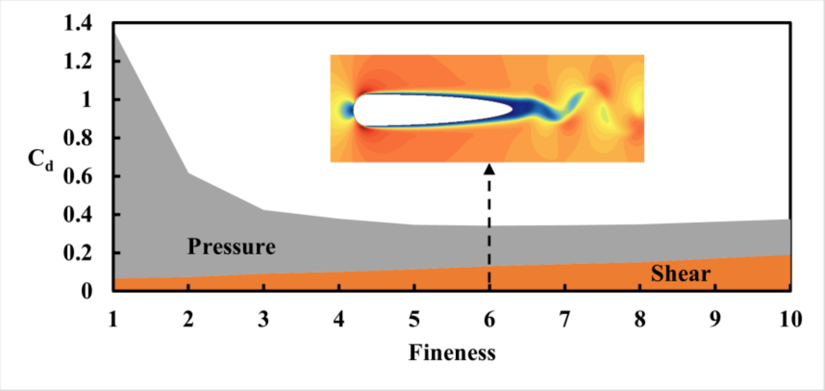

Figure 25: C_d versus fineness in freestream showing force components at Re = 6,250

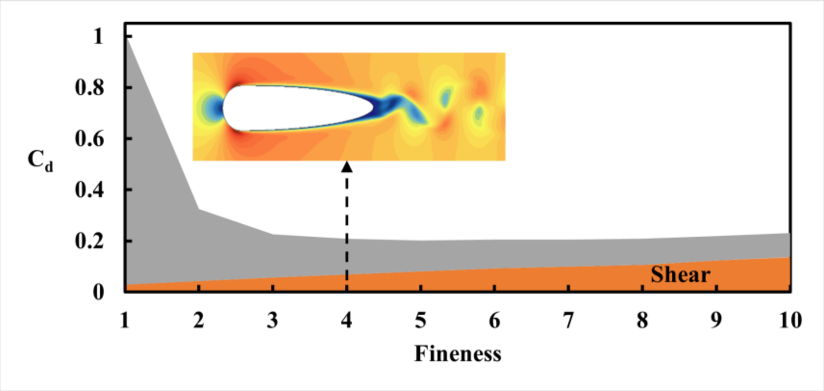

Figure 26: C_d versus fineness in freestream showing force components at Re = 22,500

4.2 Wake Fairing Characterization

4.2.1 Effect of Baseline Object

$$C_{d,combined} = \frac{D_{D-tube} + D_{fairing}}{\frac{1}{2}\rho V_\infty^2 A_{D-tube}} \qquad (13)$$

Before the full characterization, it is helpful to gain an understanding of the aerodynamics for an object with no fairing. Here, this object is taken as the fairing with a fineness of 1, resulting in a cylindrical shape. Figures 27 and 28 show the combined drag coefficient contours, calculated using equation 13, for this base shape at both Reynolds numbers. The first thing to notice is that the closer the fairing is to the D-tube, the lower the drag. Along with that, fairings of a thickness around 0.7 provide the lowest drag at these close ranges. Beyond a distance of around 1.5 diameters, this changes. At this range, the thicker fairings tend towards a lower combined drag, though only by a small amount. It should be noted that for the higher distance fairings the contour becomes more erratic as the interaction between the vortices shedding from the D-tube and the fairing becomes more complex. Altogether, it can be seen that the best case for a fairing with a fineness of 1 is as close as possible with a thickness of around 0.7 diameters.

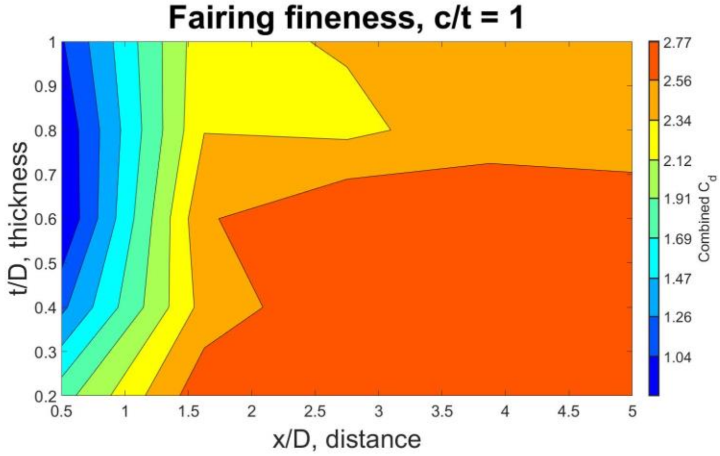

Figure 27: Contour plot of combined C_d at Re = 6,250

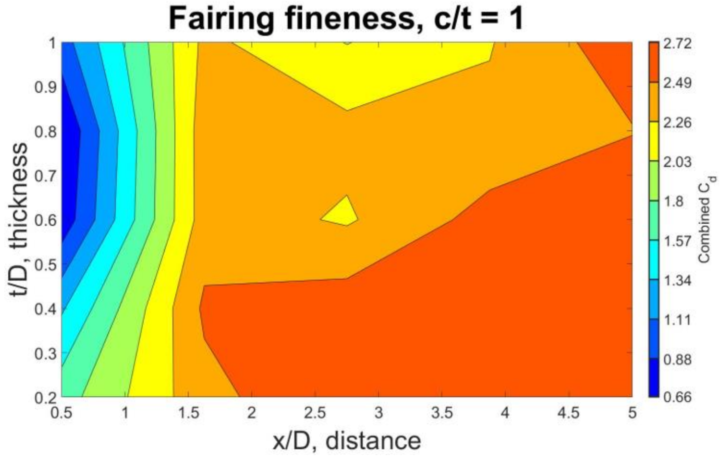

Figure 28: Contour plot of combined C_d at Re = 22,500

4.2.2 Effect of Fairing Design

The full characterization results are shown in figures 31 and 32. Similar to baseline fairing results, it can be seen that within a distance of 2.5 diameters the drag rapidly drops approaching the D-tube. Beyond that distance, however, the rate at which the drag changes is decreased resulting in a slow increase in drag further from the D-tube. Additionally, as with the baseline fairing, the drag prediction for these further distances is erratic. At higher fineness ratios this is the result of vortices from the D-tube rolling across the surface of the fairing and creating longer oscillation periods on the drag. At low fineness ratios, this behavior is also complex due to the additional formation of vortices on the fairing as it begins to resemble a bluff body and the complex interactions they create with the D-tube vortices, again leading to unsteady loads.

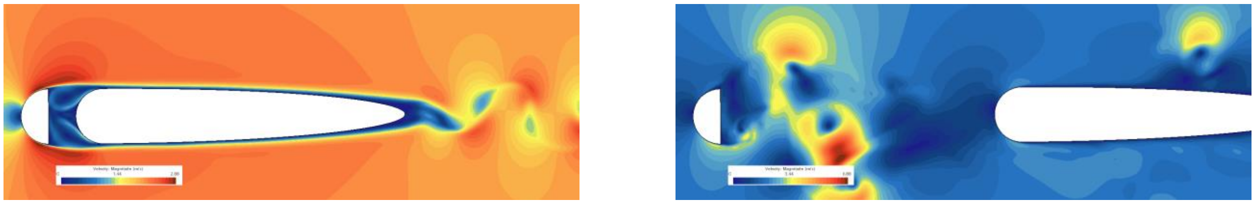

(a) x/D = 0.5

(b) x/D = 5

Figure 29: Velocity contours for fairings with c/t=6 and t/D = 1 at Re = 6,250

Focusing now on the effect of fineness, at a fixed distance and thickness, it is clear that the general behavior is that drag decreases with increasing fineness for all cases. It is important to note that the rate at which it decreases depends on the distance from the D-tube. Within a distance of around 2.5 diameters there is a consistent behavior where most of the drag decrease comes from going from a fineness of 1 to around a fineness of 3. At higher finenesses, the drag reduction slows down. Above a distance of 2.5 diameters, it consistently takes bigger increases in fineness overall to reduce drag.

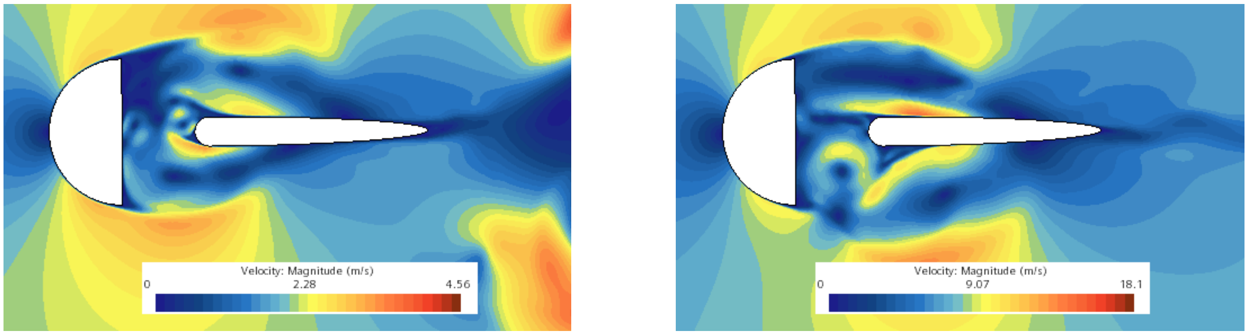

(a) Re = 6,250

(b) Re = 22,500

Figure 30: Velocity contours for fairings with c/t = 8, t/D = 0.2, and x/D = 0.5

For thickness, the effect it has is seen in the range of drag coefficients across each plot in the characterization figures and the configuration for the maximum and minimum drag, seen in Table 7. The general trend is that thicker fairings provide a lower combined drag coefficient at small distances. The reason for this can be seen in the difference in flow structure in figure 29. There, it can be seen that a thick fairing, close to the body, helps stabilize the flow separation and ends up creating regions of circulating flow instead of the constant shedding vortices seen when there is no fairing. Figure 30 shows that thin fairings bring a similar stabilization benefit, but to a lesser extent.

Table 7: Maximum and minimum drag configurations

	$C_{d,combined}$	t/D	c/t	x/D
Re=6,250	2.77	0.6	1	5
	0.28	1	8	0.5
Re=22,500	2.72	0.6	1	5
	0.2	1	8	0.5

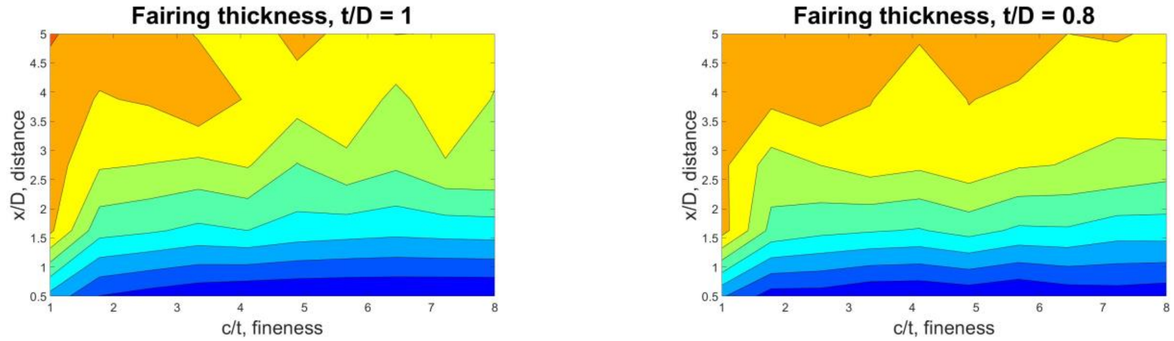

(a) t/D = 1

(b) t/D = 0.8

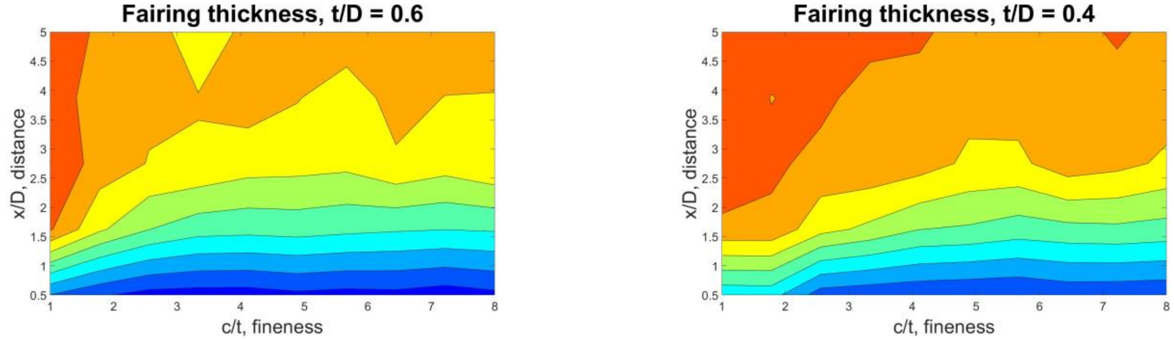

(c) t/D = 0.6

(d) t/D = 0.4

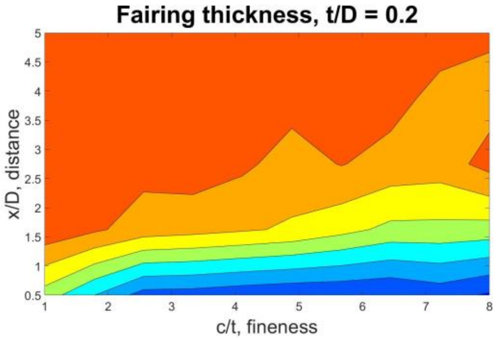

(e) t/D = 0.2

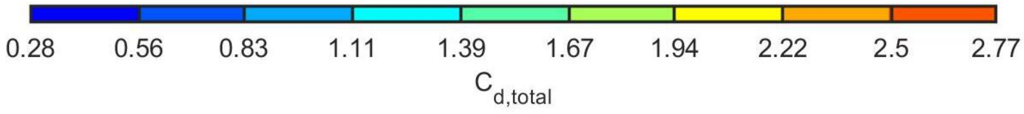

Figure 31: Total Drag Coefficient for Distance Ratio vs Fineness at Re = 6250

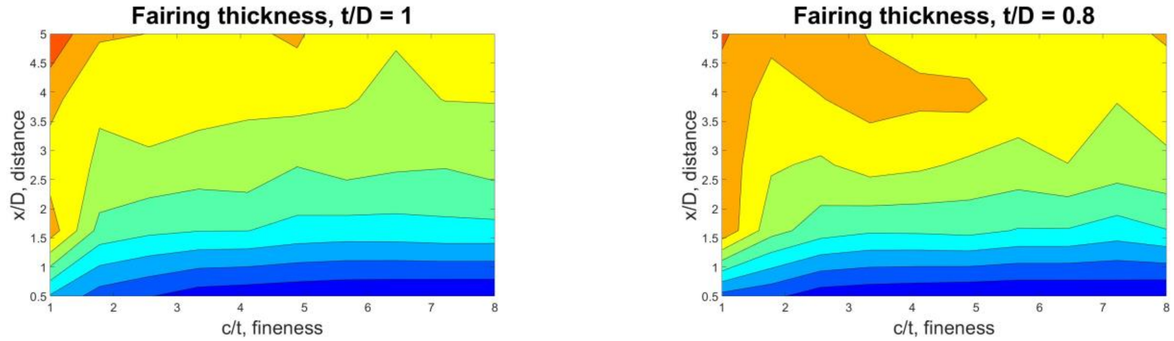

(a) t/D = 1

(b) t/D = 0.8

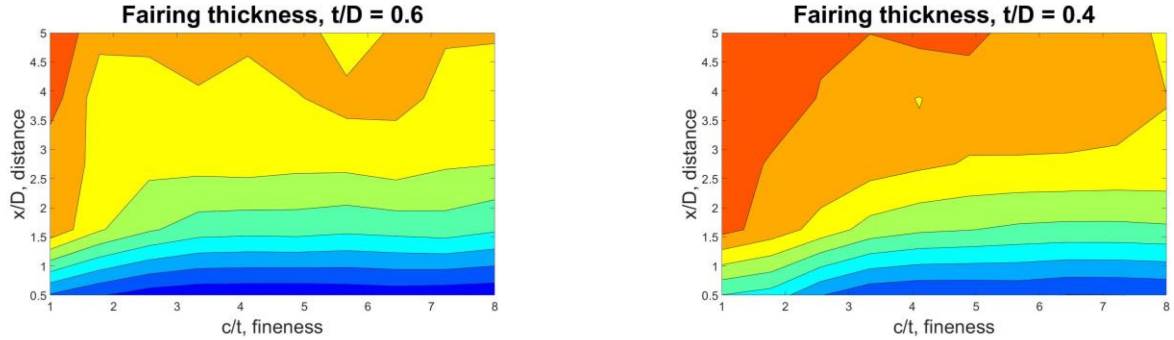

(c) t/D = 0.6

(d) t/D = 0.4

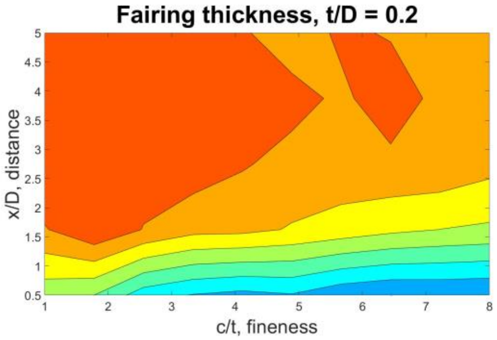

(e) t/D = 0.2

Figure 32: Combined Drag Coefficient for Distance Ratio vs Fineness at Re = 22500

4.2.3 Negative Fairing Drag and Vortex Interaction

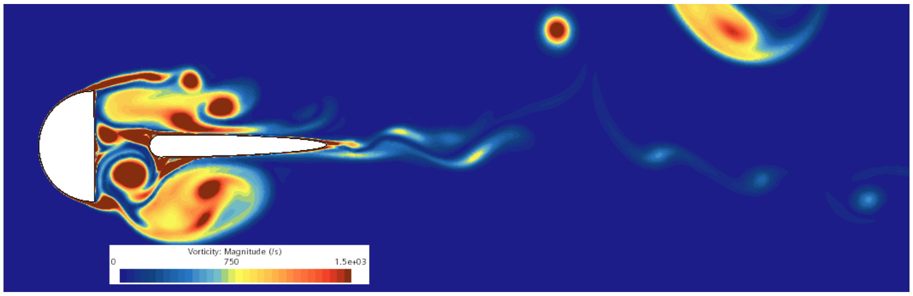

Figure 33: Vorticity contour for Re = 22,500, t/D = 0.2, c/t = 8, and x/D = 0.5

Something important to note is that though the measure for fairing characterization involved the combined drag coefficient, the isolated drag force on the fairing, though highly oscillatory in nature, was often negative or close to zero. Figure 33 gives a specific example highlighting why this happens. Here, it can be seen that the vortices shed from the D-tube create a region of recirculation, causing the flow that comes into contact with the fairing to go upstream. This in turn causes the shear component of the drag to essentially pull the fairing forward. The case is similar for fairings further from the bluff body, as seen in Figure 34, in that the shed vortices from the D-tube create a pulling frictional force upon contact with the fairing.

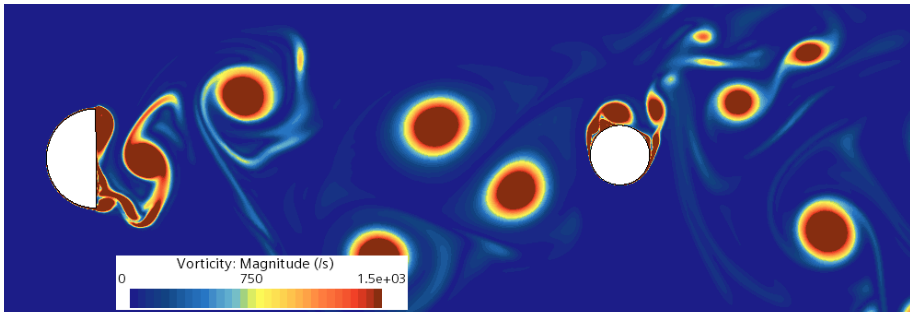

Figure 34: Vorticity contour for Re = 22,500, t/D = 0.6, c/t = 1, and x/D = 5

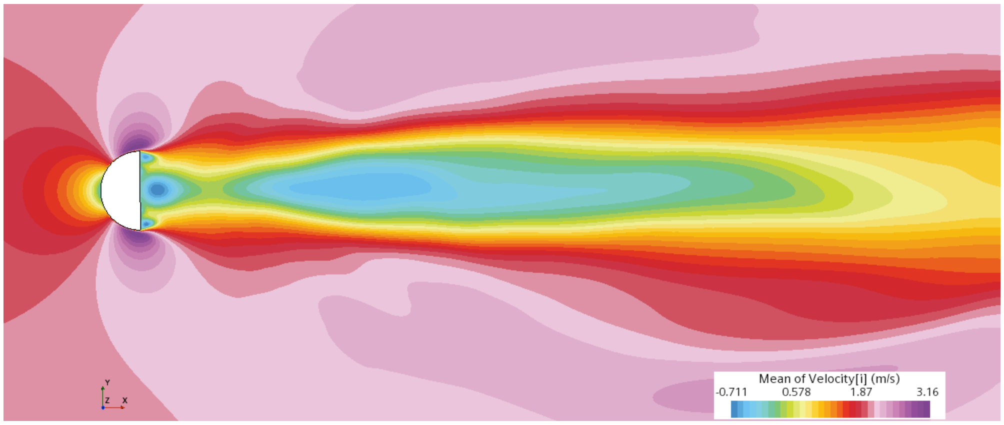

Figure 35: Time averaged velocity [i] with no fairing for Re = 6,250

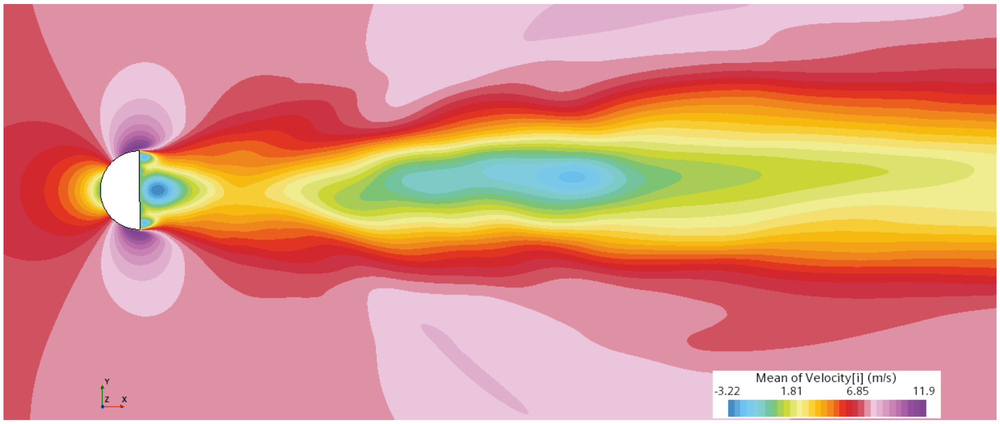

Figure 36: Time averaged velocity [i] with no fairing for Re = 22,500

Figures 35 and 36 further show how fairings close to the body can experience what can be described as a forward pull. Close to the D-tube, the time averaged velocity in the freestream direction goes upstream. Similarly, at a short distance downstream, there is another larger, though of lesser magnitude, region of reversed flow. This matches with the previously mentioned suction region that fish tend to use for entraining. The existence of the fairing does alter the location and shape of this suction region, but both the baseline fairing and the overall characterization results show that the biggest change in drag happens in this distance leading up to the suction region.

4.3 3D Fairing Example

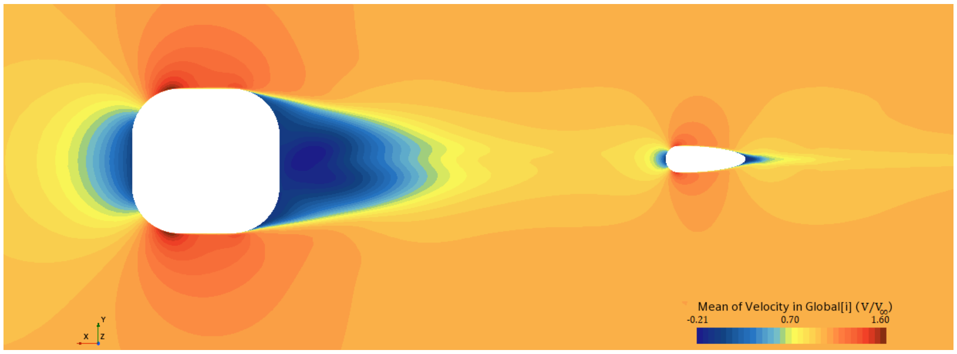

(a) Re ≈ 1.4e6 (Dragonfly cruise phase)

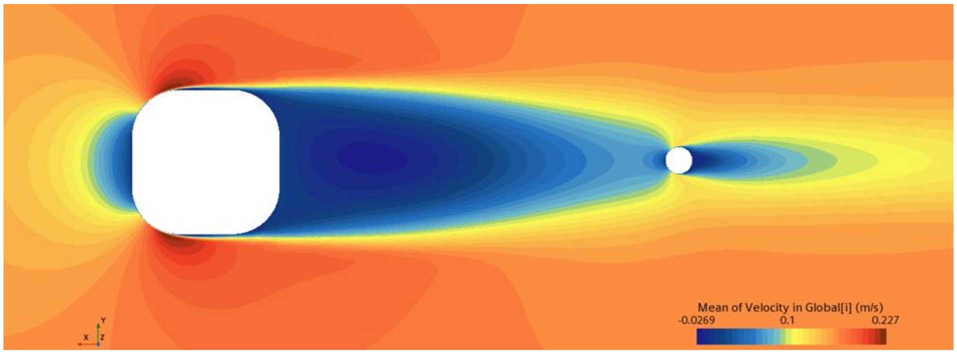

(b) Re = 22500

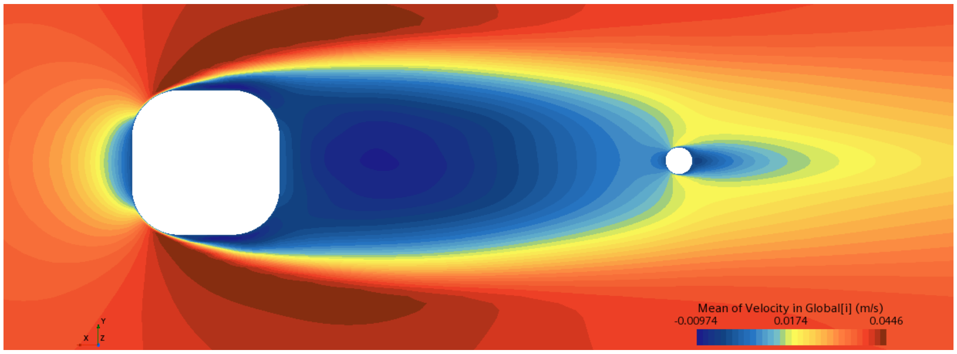

(c) Re = 6250

Figure 37: Top view cross sections of mean velocity [i] contour for a case with no fairing

The results of the three-dimensional fairing example show that there are some similarities to the two-dimensional characterization, with the exception for the case with the cruise related Reynolds number. Figures 37 and 38 show that for cruise case, the wake is much smaller, and the fairing is no longer encompassed in the wake like for the lower Reynolds numbers. This is mirrored in the drag comparisons of the LGA seen in Table 4. For both finenesses and all Reynolds numbers, adding the fairing significantly reduces drag compared to an LGA with no fairing. However, when comparing the two different finenesses directly, the cruise Reynolds number stands out. Here, the lower Reynolds numbers show that a fairing of a fineness of 7 reduces drag more than a fairing of fineness of 3. For the cruise Reynolds number, the opposite is true as the higher fineness fairing results in higher drag. In this case as the fairing is now no longer in the wake, the fairing design mirrors what would be expected with a freestream fairing design, where a fairing much larger than what is considered optimal adds drag. In contrast, the other two cases which still have the fairing fully in the wake of the bluff body mirror what is predicted in fairing design in a wake. For these two cases, increasing the fineness beyond what would be considered optimal in a freestream case still leads to reduced drag, though at a low rate compared to the increase in fairing size.

Table 8: LGA fairing drag reduction comparison

	c/t=3 vs c/t=1	c/t=7 vs c/t=1	c/t=7 vs c/t =3
Re ≈1.4e6	57.7%	54.1%	-8.4%
Re=22500	25.8%	31.4%	7.6%
Re=6250	17.4%	21.5%	4.9%

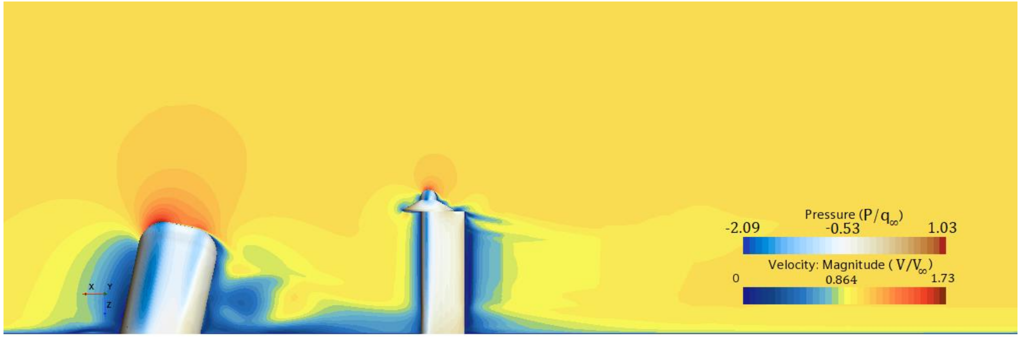

(a) Re ≈ 1.4e6 (Dragonfly cruise phase)

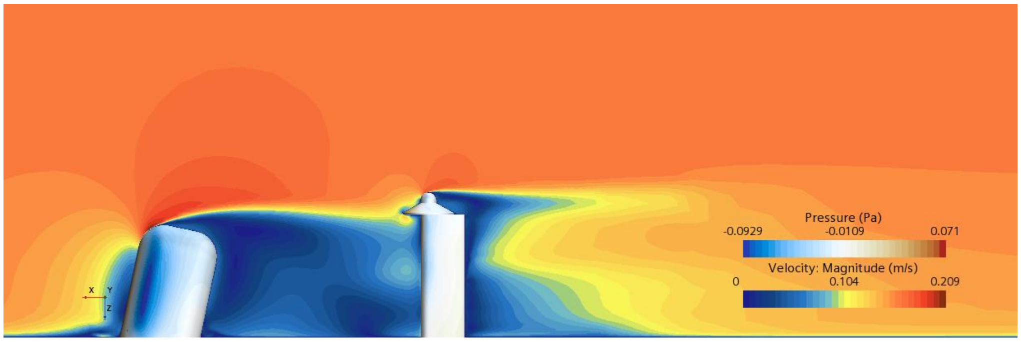

(b) Re = 22500

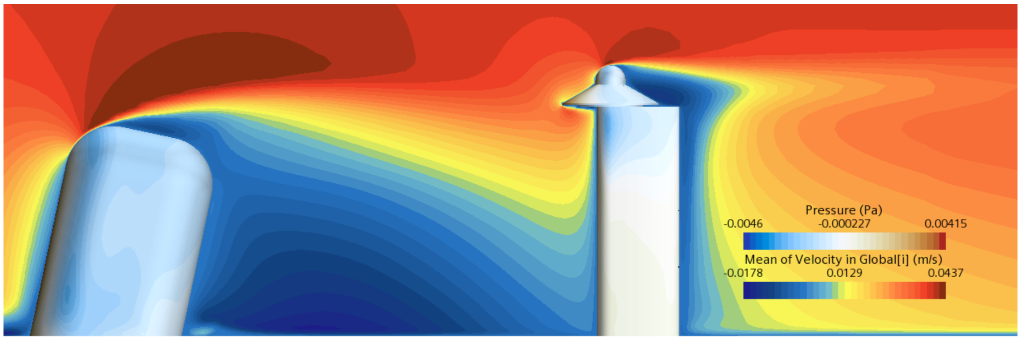

(c) Re = 6250

Figure 38: Side view cross section of velocity contours for a fairing fineness of 3

CHAPTER 5: CONCLUSION

As there is little exploration of design of a fairing in the wake of a bluff body, this paper aims to supplement this lack of knowledge by characterizing a particular case, that of an elliptical fairing in the wake of a D-tube. This was done on Star CCM+ through a two-dimensional characterization study followed by an example of how the results apply to a three-dimensional case involving NASA’s Dragonfly drone. The characterization itself involved 500 different cases at two Reynolds numbers. The results of the study showed how the changes in geometry affect a combined drag coefficient of the bluff body and fairing. In general, the trend for a design involving a D-tube in front of a fairing points towards the best design being a thick, long fairing placed close to the body. Recommendations for fairing design based off of a single parameter can also be made from the results. For distance, it is ideal to place the fairing within the range of 2.5 diameters from the D-tube, though it is preferable to have it as close as possible. Otherwise, the design is less sensitive to positioning at distances larger than 2.5 diameters. Regarding thickness, it is ideal to have a fairing of a similar size as the D-tube. Regarding the fineness, the longer the fairing is, the better, though a fineness beyond 3 has diminishing returns with respect to an increasing volume.

While these results give an idea of where optimization can start for similar cases, there is still much left to learn. Further characterization should include side forces on the fairings as those cannot be ignored and can impact design choices. Additionally, there is a necessity for studying larger ranges of the parameters explored here. For example, for the fineness it is likely that exploring higher fineness ratios than done here will reveal an optimal fineness similar to what is found for freestream streamlined shapes.

LIST OF REFERENCES

[1] Lehner, M., Whiteman, C. D., Hoch, S. W., Adler, B., and Kalthoff, N., "Flow Separation In The Lee Of A Crater Rim," *Boundary-Layer Meteorology*, vol. 173, 2019, pp. 263–287.

[2] Morel, T., "Aerodynamic Drag of Bluff Body Shapes Characteristic Of Hatch-Back Cars," *SAE Technical Paper Series*, vol. 87, Feb. 1978.

[3] Roshko, A., "On The Wake And Drag Of Bluff Bodies," *Journal of the Aeronautical Sciences*, vol. 22, Feb. 1955, pp. 124–132.

[4] Fish, F. E., "Energetics of Swimming and Flying In Formation," *Comments on Theoretical Biology*, vol. 5, Jan. 1999, pp. 283–304.

[5] Liao, J. C., and Otar, A., "A Kinematic Model Of Kármán Gaiting In Rainbow Trout," *Journal of Experimental Biology*, vol. 216, Dec. 2013, pp. 4666–4677.

[6] Phillips, A. B., Blake, J. I. R., Boyd, S. W., and Griffiths, G., "Towards Passive Station Holding Of Autonomous Underwater Vehicles Inspired By Fish Behaviour In Unsteady Flows," *Proceedings of the Institution of Mechanical Engineers, Part M: Journal of Engineering for the Maritime Environment*, vol. 230, Sep. 2015, pp. 551–565.

[7] Liao, J. C., Beal, D. N., Lauder, G. V., and Triantafyllou, M. S., "The Kármán Gait: Novel Body Kinematics Of Rainbow Trout Swimming In A Vortex Street," *Journal of Experimental Biology*, vol. 206, Mar. 2003, pp. 1059–1073.

[8] Gan, E. C., Fong, M., and Ng, Y. L., "CFD Analysis Of Slipstreaming And Side Drafting Techniques Concerning Aerodynamic Drag In NASCAR Racing," *CFD Letters*, vol. 12, Jul. 2020, pp. 1–16.

[9] Buresti, G., *Bluff Body Aerodynamics*, Italy, Genoa: University of Pisa, 2000.

[10] Mises, V. R., Kuerti, G., and Prager, W., *Theory Of Flight*, New York, New York: McGraw-Hill, 1945.

[11] Hoerner, S. F., “Drag of Streamline Bodies,” *Fluid-Dynamic Drag,* Brick Town, New Jersey: Hoerner Fluid Dynamics, 1965, pp. 15–19.

[12] *Star CCM+ User Guide,* Siemens, Munich, Germany, 2021

[13] Zienkiewicz, O. C., Taylor, R. L., Nithiarasu, P. “Incompressible Newtonian Laminar Flows” *The Finite Element Method for Fluid Dynamics* Elsevier Ltd., Waltham (2014): pp.127-161. DOI.10.1016/C2009-0-26328-8 DOI. 10.1115/FEDSM2020-20077

[14] Lienhard, J. H., Synopsis of lift, drag, and vortex frequency data for rigid circular cylinders, Pullman, Washington: Technical Extension Service, Washington State University, 1966.

[15] Ahmed, S. R., Ramm, G., and Faltin, G., “Some salient features of the time-averaged ground vehicle wake,” *SAE Technical Paper Series,* vol. 93, Feb. 1984.

[16] Guilmineau, E., “Numerical Simulation Of Flow Around A Simplified Car Body,” *Journal of Wind Engineering and Industrial Aerodynamics,* vol. 96, Jun. 2003.

[17] Ashton, N., West, A., Lardeau, S., and Revell, A., “Assessment of RANS and DES Methods For Realistic Automotive Models,” *Computers & Fluids,* vol. 128, Apr. 2016, pp. 1–15.

[18] Fey, U., König, M., and Eckelmann, H., “A New Strouhal–Reynolds-Number Relationship For The Circular Cylinder In The Range of 47<Re<2×10E5” *Physics of Fluids*, vol. 10, Jun. 1998, pp. 1547–1549.